HHS Public Access

Author manuscript

Cancer Res. Author manuscript; available in PMC 2020 June 01.

Published in final edited form as:

Cancer Res. 2019 June 01; 79(11): 2962–2977. doi:10.1158/0008-5472.CAN-18-3151.

Targeting the temporal dynamics of hypoxia-induced tumor-secreted factors halts tumor migration

Manjulata Singh[1,#], **Xiao-Jun Tian**[2,3,#], **Vera S. Donnenberg**[1,4], **Alan M. Watson**[5], **JingYu Zhang**[2], **Laura P. Stabile**[6], **Simon C. Watkins**[7], **Jianhua Xing**[2,8], and **Shilpa Sant**[1,8,9]

[1]Department of Pharmaceutical Sciences, School of Pharmacy, University of Pittsburgh, PA, USA

[2]Department of Computational and Systems Biology, School of Medicine, University of Pittsburgh, PA, USA

[3]School of Biological and Health Systems Engineering, Arizona State University, Tempe, AZ, USA

[4]Department of Cardiothoracic Surgery, University of Pittsburgh School of Medicine, McGowan Institute for Regenerative Medicine, and UPMC-Hillman Cancer Center, University of Pittsburgh, Pittsburgh, PA, USA

[5]Center for Biologic Imaging, Center for Vaccine Research, and Department of Immunology, University of Pittsburgh, Pittsburgh, PA, USA

[6]Department of Pharmacology & Chemical Biology, UPMC-Hillman Cancer Center, Pittsburgh, PA, USA

[7]Center for Biologic Imaging and the Department of Cellular Biology, University of Pittsburgh, Pittsburgh, PA, USA

[8]UPMC-Hillman Cancer Center, University of Pittsburgh, Pittsburgh, PA, USA

[9]Department of Bioengineering, Swanson School of Engineering, and McGowan Institute for Regenerative Medicine, University of Pittsburgh, Pittsburgh, PA, USA

Abstract

Targeting microenvironmental factors that foster migratory cell phenotypes is a promising strategy for halting tumor migration. However, lack of mechanistic understanding of the emergence of migratory phenotypes impedes pharmaceutical drug development. Using our 3D microtumor model with tight control over tumor size, we recapitulated the tumor size-induced hypoxic microenvironment and emergence of migratory phenotypes in microtumors from epithelial breast cells and patient-derived primary metastatic breast cancer cells, mesothelioma cells, and lung cancer xenograft cells (PDX). The microtumor models from various patient-derived tumor cells and PDX cells revealed upregulation of tumor-secreted factors including matrix metalloproteinase-9 (MMP9), fibronectin (FN), and soluble E-cadherin (sE-CAD), consistent with

Corresponding Authors: Shilpa Sant, PhD (Lead contact), shs149@pitt.edu, Phone: +1 4126489804, Address: 808A Salk Hall, 3501 Terrace Street, Pittsburgh, PA, 15261 USA. Jianhua Xing, PhD, xing1@pitt.edu, Phone: +1 4123835743, Address: Suite 3084, Biomedical Science Tower 3 (BST3), 3501 Fifth Avenue, Pittsburgh, PA, 15261 USA.
[#]These authors contributed equally to this work.

Disclosure of Potential Conflicts of Interest
Authors declare no potential conflicts of interest.

clinically reported elevated levels of FN and MMP9 in patient breast tumors compared to healthy mammary glands. Secreted factors in the conditioned media of large microtumors induced a migratory phenotype in non-hypoxic, non-migratory small microtumors. Subsequent mathematical analyses identified a two-stage microtumor progression and migration mechanism whereby hypoxia induces a migratory phenotype in the initialization stage which then becomes self-sustained through a positive feedback loop established among the tumor-secreted factors. Computational and experimental studies showed that inhibition of tumor-secreted factors effectively halts microtumor migration despite tumor-to-tumor variation in migration kinetics, while inhibition of hypoxia is effective only within a time window and is compromised by tumor-to-tumor variation, supporting our notion that hypoxia initiates migratory phenotypes but does not sustain it. In summary, we show that targeting temporal dynamics of evolving microenvironments, especially tumor-secreted factors during tumor progression, can halt tumor migration.

Keywords

Three-dimensional size-controlled microtumors; Tumor microenvironment; Hypoxia; Hypoxic/tumor secretome; Soluble E-cadherin (sE-CAD); Bistable switch

Introduction

Metastases to distant organs are the major cause of mortality in cancer patients (1,2). For solid epithelial-stromal tumors, epithelial cells acquire a migratory phenotype, break away from the primary tumor, navigate through the extracellular matrix, and extravasate into the circulation to form secondary metastases (3,4). Therefore, mechanistic understanding of the emergence of migratory phenotypes is important for identifying novel and effective treatment strategies to prevent metastases.

Tumor epithelial cells interact with the extracellular matrix and the neighboring tumor, stromal and immune cells. They are exposed to various secreted factors presented in the local microenvironment, and they themselves shed/secrete various factors (secretome) to actively reshape the microenvironment, which in turn contribute to phenotypic plasticity and tumor progression (2,5,6). Hence, increasing number of emerging cancer treatments target secreted factors in tumor microenvironment (7–9). Unlike molecular therapies targeting the tumor cells, those targeting the microenvironments including tumor-secreted factors are expected to be less prone to adaptive changes in the tumor cells and thus, emergence of resistant cell populations (7). However, success of such therapies remains mixed. For example, hypoxia is known to contribute to hypoxic secretome (10) and activate several transcription factors (1) and epigenetic modifications (11). These can further induce cell phenotype changes such as conventional or partial epithelial-to-mesenchymal transition (EMT) that contributes to drug resistance and possibly, to tumor migration and metastasis (3,11–17). However, hypoxia-targeted therapies combined with current standard-of-care therapies (*e.g.,* chemotherapy or radiotherapy) showed mixed outcomes in several clinical trials (18–20). This failure is not so unexpected since tumor cells can maintain their aggressive behavior in non-hypoxic conditions after they extravasate away from the tumor mass, and thus, may not be affected by an anti-hypoxic therapy applied after tumor

migration program is turned on. Therefore, an effective treatment strategy needs to tackle the intricate regulatory network that initiates, and maintains the tumor migratory phenotype (21).

Since hypoxia is one of the microenvironmental parameters implicated in inducing migratory phenotype and associated therapy resistance, it is important to have an experimental system that recapitulates spontaneously formed hypoxic microenvironment along with the tumor secretome. Traditional two-dimensional (2D) cell culture-based assays are unable to capture the constantly evolving dynamic *in vivo* microenvironment and are likely poor surrogates for studying emergence of migratory phenotypes (see recent review (13)). Typical *in vitro* 3D cultures such as spinner flasks (22–24) generate a broad size distribution of multicellular aggregates (microtumors), which presents a technical difficulty for systematically studying the effect of tumor size-induced hypoxic microenvironment. To engineer controlled local microenvironment that is purely defined by microtumor size and tumor-secreted factors, we adopted microfabricated hydrogel microwells to generate hundreds of microtumors of uniform yet precisely controlled sizes from multiple cancer cell lines including breast, prostate and head and neck cancer (24–28). Precise control over microtumor size translated in controlled hypoxic and metabolic microenvironments (25–28). By manipulating microtumor size alone and without any genetic manipulations or exogenous stimuli, we reproducibly generated two distinct phenotypes from the same non-invasive parent breast cancer cells: small non-hypoxic microtumors represent non-migratory phenotype whereas large hypoxic microtumors exhibit migratory phenotype (25,26,28). Notably, the migratory cells in large microtumors could remember their phenotype and remain migratory even after dissociating into single cell suspension and re-growing into small non-hypoxic microtumors (25). Therefore, our microtumor model recapitulates both, hypoxia-induced migratory phenotype in large microtumors and its subsequent maintenance under hypoxia-free microenvironment in small non-hypoxic microtumors.

The objective of this study was to investigate the mechanisms involved in the acquisition of migratory phenotype by the parent non-invasive breast cancer cells and its maintenance under hypoxia-free microenvironment using size-controlled microtumor models. We used only monocultures of tumor cells without other stromal cells to delineate hypoxia-induced changes in the tumor secreted factors to generate migratory phenotypes in pre-invasive parent cells. A tangible advantage of our microtumor platform is the ability to precisely and reproducibly study how the hypoxic microenvironment induces tumor migration in real time and in isolation from non-tumor cells present *in vivo*, providing unique opportunity to define tumor-intrinsic mechanisms of transition from non-migratory to migratory phenotype. We demonstrate a two-stage tumor progression mechanism that tumor size-induced hypoxia induces migratory phenotype in the initialization stage, which is subsequently maintained by feedback loop among tumor-secreted factors such as MMPs/sE-CAD/FN. We provide compelling evidence that targeting molecules involved in the maintenance stage, but not in the initialization axis of tumor progression, can be an effective treatment strategy that is less affected by tumor progression stage.

Materials and Methods

Chemicals and Reagents

All chemicals and reagents were procured from Sigma-Aldrich (Milwaukee, USA) unless specified. All antibodies were purchased from Santa Cruz Biotechnology (California, USA) except anti-Vimentin (MA3–745), anti-beta actin (MA5–15739) from Thermo Scientific Inc. (Rockford, USA); anti-ERK (9102S) and, anti-pERK (4370P) from Cell signaling Technologies Inc. (Massachusetts, USA); anti-HIF1-α (GTX127309) from GenTex (California, USA) and anti-Fibronectin (610077) from BD Biosciences (California, USA). GM6001 (MMP inhibitor) was procured from Millipore (Ontario, Canada) and Methyl 3-[[2-[4-(2-adamantyl) phenoxy] acetyl]amino]-4-hydroxybenzoate (HIF1-α inhibitor) was obtained from Santa Cruz Biotechnology (California, USA). Human E-Cadherin Quantikine ELISA Kit was purchased from R&D Systems (Minneapolis, USA).

Cell lines and cell culture

Breast cancer cell line T47D was purchased from American Type Culture Collection (ATCC) and cell culture supplies and media were obtained from Corning® and Mediatech®, respectively unless specified. T47D cells were passaged and maintained in T75 flasks in Dulbecco Modified Eagle Medium (DMEM) (supplemented with 10% fetal bovine serum (FBS) (Hyclone, Utah, USA) and 1% penicillin-streptomycin in 5% CO_2 at 37 °C in a humidified incubator. Cell line authentication was done by University of Arizona, Genetics Core by using PowerPlex16HS PCR Kit. Briefly, genomic DNA was genotyped for 15 Autosomal STR loci and Amelogenin using Promega Power Plex16HS PCR kit and the electropherogram were analyzed using Soft Genetics, Gene Marker Software Version 1.85. Alleles were matched to STR profile and a minimum of 80% match threshold was used for standardization of STR Profiling and shared genetic history using ANSI database. Cells were maintained to attain 40–60% confluence for further seeding into hydrogel microwell devices.

Primary cell cultures of malignant pleural effusions

Pleural effusions were collected from patients with metastatic breast cancer (mBC) or mesothelioma as waste materials during therapeutic drainage. Samples were anonymized by an honest broker and provided along with relevant clinical information, to the laboratory according to University of Pittsburgh IRB exemption (0503126, VSD). The cells were cryopreserved in 1.25mL vials (~50×10^6 cells/vial) in MEM containing 10% DMSO and 20% calf serum. The cryopreserved cells were carefully thawed in ice cold DMEM supplemented with 50% calf serum, suspended in complete mammary epithelial growth medium (MEGM, Catalog #CC-3151, Lonza, Walkersville, MD) supplemented with 10% fetal bovine serum (Catalog #SH30088.03, HyClone GE Healthcare Life Sciences) and 10% autologous cell-free pleural fluid. Complete MEGM consists of Epithelial Cell Basal Medium supplemented with bovine pituitary extract (BPE, Lonza Catalog #CC-4009G) human epidermal growth factor (rhEGF, 10ng/mL, Lonza Catalog #CC-4017G), hydrocortisone (0.5μg/mL, Lonza Catalog #CC-4031G), gentamicin sulfate plus amphotericin B (Lonza Catalog #CC-4081G) and insulin (10μg/mL, Lonza Catalog #CC-4021G). The cells were initially plated in 10 cm petri dishes at a culture density of 1 –

1.5 ×10^5 cells/cm^2, grown to semi-confluence, trypsinized and split 1 to 3. All samples were analyzed at passage 0 and 1.

Multicolor flow cytometry on unpassaged metastatic breast cancer samples (MPE175)

Detailed methods used to disaggregate, stain and analyze unpassaged metastatic breast cancer samples have been described in detail (29). Non-specific binding of fluorochrome-conjugated antibodies was minimized by pre-incubating pelleted cell suspensions for 5 min with neat decomplemented (56°C, 30 min) mouse serum (5μL) (30). The cells were then pelleted again by centrifugation and residual fluid aspirated. All antibodies were added at a fixed volume (2μL) representing an approximate dilution of 1:5. Cells were first stained for surface markers. The order of addition was: CD326/EpCAM-APC (Miltenyi Catalog #130-098-118) CD45-APCCy7 (BD Biosciences, Catalog #348805), CD44-PECy7 (Abcam, Cambridge, MA, Catalog #ab46793), CD90-APC (BD Biosciences, San Jose CA, Catalog #559869), CD14-PECy5 (Beckman-Coulter, Brea CA, Catalog #IM2640U), CD33-PECy5 (Beckman-Coulter, Catalog #IM2647U) and Glycophorin A-PECy5 (BD Biosciences, Catalog #559944), CD73-PE (BD Pharmingen, Catalog #550257). Unbound antibodies were washed and cells were fixed with 2% methanol-free formaldehyde (Polysciences, Warrington, PA). Cells were then permeabilized with 0.1% saponin (Beckman Coulter) in phosphate buffered saline with 0.5% human serum albumin (10 min at room temperature); cell pellets were incubated with 5μL of neat mouse serum for 5 min, centrifuged and decanted. The cell pellet was disaggregated and incubated with 2μL of anti-pan cytokeratin (CTK, Abcam, Catalog #ab52460) and vimentin-(VIM, BD Pharmingen Catalog #562338) for 30 min. Cells pellets were diluted to a concentration of 10×10^6 cells/400μL of staining buffer and DAPI (Life Technologies, Grand Island NY, Catalog #D1306) was added 10 min before sample acquisition, to a final concentration of 7.7μg/mL and 40μL/10^6 cells. In this application, DAPI was used as a DNA stain in fixed permeabilized cells because it permits removal of artifacts associated with tissue digestion and also provides information on cell DNA content. Stained cells were acquired on a Beckman Coulter Gallios cytometer calibrated to pre-established PMT target channels. Offline compensation and analyses were performed using VenturiOne software (Applied Cytometry, Dinnington, Sheffield, UK) as detailed previously (30). Spectral compensation matrices were calculated for each staining combination within each experiment using single-stained mouse IgG capture beads (Becton Dickinson, Catalog #552843) for each tandem fluorochrome, and BD Calibrite beads for PE and APC controls (Becton Dickinson, Catalog #340486).

3D culture and microtumor fabrication

Non-adhesive hydrogel microwell devices of 150 and 600μm were microfabricated using polyethylene glycol dimethacrylate (PEGDMA, 1000Da) and polydimethyl siloxane (PDMS) molds as described previously (25,26). PDMS molds with 150 and 600μm posts (1:1 aspect ratio of height: diameter) were placed on PEGDMA solution (20% w/v) mixed with photoinitiator (Irgacure-1959, 1% w/v, Ciba AG CH-4002, Basel, Switzerland) and photo-crosslinked using the OmniCure S2000 curing station (EXFO, Mississauga, Canada). Subsequently, T47D cell suspension in growth media (200μL, 4.0 × 10^6 cells/device) was seeded on the 2×2 cm^2 hydrogel microwell device and cultured in a humidified 5% CO_2 incubator. Microtumors were cultured up to 6 days with replacement of 50% media with

equal amount of fresh media every day and harvested on day 6 and processed further as required or frozen at −80 °C. Methods for isolation of primary cells from primary metastatic breast cancer (mBC), mesothelioma and patient-derived mouse xenograft (PDX) as well as fabrication of 3D microtumors from these primary tumor cells and xenografts is described in Supplementary Information (Materials and Methods).

Clinical data for FN and MMP9 expression in patient tumors

For FN1 and MMP9 expression profile analysis in patient tumors, we integrated high quality metadata of human that were obtained by AffyU133Plus2 platform expression arrays from public repositories, such as GEO. 3735 Homo sapiens samples were included in the results. The original targeted gene expression profile in nine subcategories of cancers as well as normal tissue was extracted and normalized by Genevestigator®.

Treatment of microtumors with conditioned media (CM) and various inhibitors

To study the effect of hypoxic secretome, 150μm microtumors were treated with conditioned media of 600μm microtumors (denoted as “600/CM”) from day 3 to day 6. To investigate the role of soluble E-CAD (sE-CAD) on microtumor migration, 150μm microtumors were treated with recombinant human E-CAD, Fc chimera protein (20 μg/mL, R&D Systems, Minneapolis, USA) for pre-determined time.

HIF-1α was inhibited chemically by treatment of 600μm microtumors with growth media containing HIF-1α inhibitor, methyl 3-[[2-[4-(2-adamantyl) phenoxy] acetyl] amino]-4-hydroxybenzoate (1.0μM) at different time points. MMP inhibition was achieved by treating the 600μm microtumors with of broad spectrum MMP inhibitor (GM6001, 20μM). To scavenge sE-CAD secreted in the conditioned media, 600μm microtumors were treated with ectodomain antibody (H-108, 40μg/mL, Santa Cruz Biotechnology) in the growth media from day 3 to day 6 or day 4 to day 6.

After CM and various inhibitor treatment studies, mRNA were isolated from control (untreated) and treated microtumors and EMT marker expression was determined by qRT-PCR. Similarly, protein expression was estimated by western blotting.

Kinetics of microtumor migration

The aggressive phenotype of microtumors was assessed by measuring the distance of migration (d) and extent of migration (%), respectively. The distance of migration (d) was estimated by measuring the average length of straight-lines drawn perpendicular to periphery of the well up to the leading edge, covering the entire migratory front using ImageJ. Of note, distance of migration for each microtumor was average of approximately ≥ 10 such perpendicular lines and was represented as the distance in microns. The extent of migration is the percentage of the area of the microtumor that is migrated out of the microwells ($A_{Migration}$) normalized with the total area of the microtumor (A_{Total}), [extent = $A_{Migration}$/ A_{Total} *100]; (see Fig. 1A) and was measured by ImageJ using analyze > set scale> Ctrl+T> measure tools.

Protein extraction and western blotting

Frozen microtumor samples were lysed in radioimmunoprecipitation assay (RIPA) buffer containing Tris (50mM, pH 7.4), sodium chloride (150mM), sodium deoxycholate (0.5%), NP-40 (1%), phenylmethane sulfonyl fluoride (0.05mM), and protease inhibitor cocktail for mammalian tissue extract and phosphatase inhibitor (Sigma-Aldrich Inc., Milwaukee, USA). Proteins secreted in the conditioned media (sE-CAD and FN) were measured by resolving 50 μL of conditioned media on 8–10 % polyacrylamide gel, transferring them to PVDF membrane and probing them with respective antibodies. Of note, CM of 150 and 600 μm microtumors were collected from the hydrogel microwell devices that have same number of cells. To match the cell number of 150 and 600 μm microwell devices, cells/microtumor was calculated for both 150 and 600 μm microtumors. Subsequently, the dimensions of each device were adjusted to contain number of microtumors totaling to the same total cell number/device. Western blot was performed for primary antibodies against Vimentin (1:1000), Fibronectin (1:1000), E-CAD (1:1000), pERK (1:1000), ERK (1:1000), and β-actin (1:2000) as described previously (25). Membranes were scanned by Odyssey Infrared Imaging System (LI-COR® Biosciences, Lincoln, USA) and colored images were converted to grayscale images by using Odyssey 3.0 software. Quantification of blots was done by ImageJ Software (National Institute of Health, USA) and normalization of densitometry was done by comparing with β-actin. The data are expressed as fold change compared to control/600 (n=3).

Measurement of shed sE-CAD in the conditioned media by ELISA

sE-CAD levels in the conditioned media (CM) of 150 and 600μm microtumors and inhibition studies were measured by quantitative ELISA (R&D Systems, DCADE0) according to the manufacture's protocol. Of note, CM of 150 and 600 μm microtumors were collected from the hydrogel microwell devices that have same number of cells as mentioned above for western blotting. All the CM were diluted (1:2) using dilution buffer from the kit before assay as described in the instruction manual. The standards and samples (50μL) were pipetted into the E-CAD antibody pre-coated wells of microplate and incubated for 2h at room temperature on rocking platform. Any unbound material was removed by four times washing with wash buffer, an enzyme-linked polyclonal antibody specific for E-CAD was added to the wells and incubated for 2h at room temperature on rocker. Any unbound antibody-enzyme reagent was washed with wash buffer, followed by addition of a substrate solution and incubation for 30 min to develop the color. The reaction was stopped using stop solution and absorbance was measure at 450nm. Each sample was measured in duplicate. The concentrations of sE-CAD were determined by extrapolating the values on the standard curve followed by multiplication of dilution factor and represented as ng/mL.

Immunostaining and confocal microscopy

E-Cadherin-GFP expressing microtumors were cleared using CUBIC R1 (31). The clearing solution was removed by washing with CUBIC IHC buffer (phosphate buffered saline, PBS; 0.1% Triton X-100; 0.5% bovine serum albumin, BSA; 0.01% Sodium Azide) and then stained with anti-Vimentin (Abcam, ab73159) for 24h. Samples were then washed and incubated with anti-chicken-Cy5 for 24h (Jackson ImmunoResearch, 703-175-155).

Samples were washed again and placed in CUBIC R2 without triethanolamine (32) containing Hoechst for 24h prior to imaging. All incubation steps were done at 37°C with gentle movement. The immunostaining protocol was optimized to ensure antibody penetration throughout the volume of microtumors. Volumes were acquired over whole microtumors using a Nikon Ti-E equipped with a Bruker SFC and excitation at 405, 488 and 640 nm. The Voxel size was 0.4 × 0.4 × 5.0μm using an Apo 40x WI λS DIC N2 objective. Images were prepared in NIS Elements v4.51.00. Preparation of publication quality images included rolling ball background correction and local contrast enhancement.

RNA isolation and qRT-PCR analysis

RNA was isolated from all the samples by using GeneJET RNA purification kit (Thermo Scientific, Lithuania, EU) as per manufacturer's protocol. RNA quantity was measured by absorbance ratio at 260/280 nm and integrity was verified on 1% agarose gel. The mRNA expression of EMT markers such as Vimentin (*VIM*), Fibronectin (*FN*) and E-cadherin (*E-CAD*) and matrix metalloprotease 9 (*MMP9)* was analyzed by qRT-PCR using iTaq Universal SYBR Green One-Step RT-PCR kit (BioRad Laboratories Inc., USA) and 7500 Fast Real-Time PCR System (Applied Biosystems, California, USA) using β-Actin as control house-keeping gene. The mRNA expression was quantified using the $2^{-\Delta\Delta Ct}$ and presented as the mean ± SEM as fold change compared to controls (150 or 600μm microtumors). Primer sequences are given in Supplementary Table S1.

Gelatin zymography

MMPs are responsible for cleavage of ectodomain E-CAD to generate 80 kDa sE-CAD. To estimate the levels of MMPs in the CM, gelatin zymography was performed as described by Frankowski et al. (33). Briefly, 50μL of CM was mixed with non-reducing sample buffer and separated on 7% polyacrylamide gel containing 1.0% porcine gelatin Type A (Sigma). Gel was washed thrice using wash buffer containing 25% v/v Triton X-100. Subsequently, the gel was incubated in developing buffer containing 50mM Tris, 10mM CaCl2 and 0.02% sodium azide, for 48h at 37°C. Staining was done for 40 min using Coomassie Blue staining solution and destaining was done until the bands appeared. Imaging was done using GelDoc (BioRad) and quantification was done by densitometric analysis of bands by ImageJ.

Statistical analysis

Statistical analysis was done using GraphPad Prism7. All the values were presented as mean ± SEM. Unpaired t-test was used to compare the significance between two groups. For multiple comparisons (effects of inhibitor treatments), data were analyzed by one-way analysis of variance (ANOVA) followed by a Tukey's test. A *p*-value less than 0.05 was considered significant.

Mathematical modeling and analysis

A set of ordinary differential equations (ODEs) to model the N-terminal E-cadherin shedding is applied in the theoretical analysis (details can be found in the Supplementary material). The model quantitatively captures the dynamics of the core regulatory network that governs the N terminal E-cadherin shedding in hypoxic microenvironment. The default

state is the non-migratory phenotype, in which the levels of the HIF-1α, MMPs and sE-CAD are low. The quantitative model consisted of 4 ODEs with 20 kinetic rate parameters (Supplementary Table S2). The bifurcation analysis was performed with the software Oscill8 (http://oscill8.sourceforge.net/). For HIF-1α inhibition simulation, the HIF-1α-mediated expression rate of MMPs is set to 1/10 of its original value while for the sE-CAD inhibition, the sE-CAD-mediated expression rate of ERK is set to 1/10 of its original value. For the MMP inhibition, the shedding rate of sE-CAD mediated by MMPs is set to 1/10 of its original value. All the concentrations are in a reduced unit. More detail is provided in SI materials and methods.

Results

Large microtumors exhibit hypoxia, collective migration and aggressive phenotype

We adopted our microfabricated hydrogel microwell platform (25,26) to generate uniform size T47D microtumors of 100–120μm (referred as 'small' microtumors) and 500–600μm in diameter (referred as 'large' microtumors). We selected 150 and 600μm microwells to engineer non-hypoxic and hypoxic microenvironments based on our previous studies (25,26,28) as well as clinically reported tumor lesion sizes (34).

We cultured small and large size-controlled microtumors of non-invasive human T47D cells in microwell arrays for six days. While small microtumors remained non-migratory after six days in culture, large microtumors moved towards the wall of the microwells and showed collective migration out of the wells (Supplementary Fig. S1Ai and ii, Supplementary Video) starting from day 3. Both small and large microtumors exhibited similar rate of proliferation (about 1.5–2 fold) (28), ruling out the differences in proliferation or cell crowding in the microwell as the cause of migration. We quantified the distance of migration (d), area of the migrated portion ($A_{Migration}$), and total microtumor area (A_{Total}) using ImageJ (Fig. 1A). Despite highly homogeneous size distribution on the same 2×2 cm^2 device, we observed microtumor-to-microtumor variation in the migration kinetics of large microtumors, parallel to the well-documented cell-to-cell variation (35). We quantified observed variations in migration kinetics of individual microtumors by the migrated distance (d) and the extent of migration ($A_{Migration}/A_{Total}$*100) (Fig. 1B–C, Supplementary Fig. S1B). We conjectured that the different behaviors of 150 and 600μm microtumors result from size-associated changes in their microenvironments. Therefore, we measured intra-tumoral expression of hypoxia-inducible factor 1 alpha (HIF-1α), EMT markers (vimentin, VIM and fibronectin, FN) and levels of tumor-secreted factors including matrix metalloproteinases (MMPs), FN and soluble E-cadherin (sE-CAD) in the conditioned media (CM). We observed upregulation of HIF-1α protein in cell lysate (Supplementary Fig. S1C) and upregulation of mesenchymal markers, VIM and FN without loss of epithelial marker, E-CAD (Supplementary Fig. S1D) suggesting that the migratory behavior of large microtumors represents "cohesive or collective migration" that requires E-CAD (4,36). Indeed, immunostaining of large T47D microtumors showed presence of E-CAD+/VIM+ cells at the periphery without loss of E-CAD (Supplementary Fig. S1E, white arrows). Large microtumor CM showed increased levels of sE-CAD (Fig. 1D–E), FN, Pro-MMP9 and MMP9 compared to the small ones (Fig. 1E). The downstream extracellular signal-regulated

kinase (ERK) was activated as shown by upregulation of pERK in large microtumors (Fig. 1F). These results indicate that large tumor size induces hypoxic tumor microenvironments, higher levels of tumor-secreted factors (sE-CAD, FN, MMP9) and collective migration possibly due to the acquisition of mesenchymal features without loss of E-CAD. Interestingly, we observed intra-tumoral differences in E-CAD and VIM expression along with inter-tumoral differences in migration kinetics in large microtumors.

Hypoxic tumor CM contain factors that can induce collective migration in non-hypoxic, non-migratory small microtumors

Next, we asked whether hypoxia alone is responsible for inducing the migratory phenotype in large microtumors. In our previous work, HIF-1α knockdown in large microtumors either by siRNA or pharmacological inhibition from day 1 downregulated expression of mesenchymal markers and suppressed migration in large microtumors (25), suggesting possible role of hypoxic pre-conditioning and HIF-1α stabilization in migration as suggested by others (37,38). When non-hypoxic small microtumors were dissociated into single cells and re-grown into large ones, they acquired migratory phenotype, confirming the role of hypoxic microenvironment in migration (25). Interestingly, when large microtumors were dissociated into single cells to remove the hypoxic microenvironment and re-grown into small microtumors, they sustained their migratory phenotype (Fig. 2A). This suggests that the hypoxia-induced migratory phenotype is not reversible even after removal of hypoxic microenvironment. Our observation that environmental pre-conditioning (such as hypoxia) may predispose to aggressive tumor progression is consistent with previous studies showing that tail vein injection of tumor cells exposed to hypoxic conditions, followed by re-oxygenation, resulted in increased metastasis (16,17). We hypothesized that the hypoxic CM of large microtumors (600/CM) contain factors that contribute to maintain the migratory phenotype. When treated with 600/CM from day 3–6, 60% of otherwise non-hypoxic, non-migratory small microtumors became migratory (Fig. 2B–C).

The 600/CM contain multiple factors. Although we did not perform full secretome analysis, 600/CM showed elevated levels of sE-CAD compared to the 150/CM (Fig. 1D–E). Treatment with recombinant human sE-CAD (Rec-sE-CAD) also induced migration in more than 60% small microtumors (Fig. 2B–C). Both, 600/CM and Rec-sE-CAD treatments induced collective migration without loss of E-CAD (green, Fig. 2B). sE-CAD is known to upregulate MMP expression (39). Indeed, both 600/CM- and Rec-sE-CAD-treated 150μm microtumors showed more than 8-fold increase in *MMP9* expression (Fig. 2D). 600/CM-treated small microtumors showed significantly upregulated *FN* (4.0±0.9 fold) and *VIM* (5.0±2.9 fold), while those treated with Rec-sE-CAD significantly upregulated only *FN* (8.6±2.7 folds) with no effect on *VIM* (Fig. 2E). These results confirmed that either 600/CM or sE-CAD alone could induce the migratory phenotype in non-migratory (150μm) epithelial microtumors albeit they have differential effects on regulating *VIM* expression. In comparison, 150/CM did not affect migratory behavior of either small or large microtumors (Supplementary Fig. S2A–B). While our data demonstrates the role of 600/CM in inducing migratory phenotype in non-migratory small microtumors, other possible mechanisms such as epigenetics may also contribute to the emergence and maintenance of the migratory phenotype.

Patient tumors, as well as microtumors of primary patient-derived tumor cells and PDX cells show upregulation of FN, MMP9 and sE-CAD in their secretome

To investigate the clinical relevance of FN and MMP9, we extracted clinical data from various breast cancer types from a set of 3735 human samples by Genevestigator® and analyzed them with AffyU133Plus2. Expression of FN and MMP9 were higher in various breast carcinomas compared to the normal mammary gland (Fig. 3A). Furthermore, we fabricated small and large microtumors using primary cancer cells derived from fresh metastatic breast cancer (mBC, one patient sample), mesothelioma (one patient sample) and lung PDX-derived cells (two patient samples) (Fig. 3B). Representative photomicrographs of malignant pleural effusions used in this study are shown in Supplementary Fig. S3 and S4. Despite the metastatic and highly invasive nature of malignant pleural effusions, morphological characterization of mBC cells revealed microtumor clusters (Supplementary Fig. S3A). Flow sorted aneuploidy tumor cells revealed mixed population of cytokeratin (CTK)+/VIM+ and only VIM+ cells with small subpopulation of cells expressing surface mesenchymal markers (CD44, CD90) (Supplementary Fig. S3B–C). Patient- and xenograft-derived primary cancer cells formed small and large microtumors in our microwell arrays, albeit, the microtumor sizes immediately after seeding were smaller than breast cancer cell line-derived microtumors (Supplementary Fig. S4A–C). This could be attributed to the differences in the cell size and compaction ability of individual cells isolated from different tumors. We have reported similar observations with head and neck cancer cell lines (25,26). Notably, the microtumors of primary cancer cells from different tumor types also recapitulated the results obtained with the breast cancer cell lines, where large microtumors showed migratory phenotype on day 6–8 while smaller ones remained non-migratory. Compared to the small microtumors, the large microtumors of patient-derived mBC cells showed 4-fold upregulation of *FN* with a slight but not significant change in *VIM* mRNA (Fig. 3C). Interestingly, we also observed significant downregulation of *E-CAD* and *MMP9* mRNA (Fig. 3C, D). This could be because the primary mBC cells are derived from highly metastatic pleural effusions and may have molecular subtype different than T47D cells. Despite the microtumor clusters present in mBC pleural effusions as shown here, the mesenchymal phenotype is predominant (30). We also observed increased levels of sE-CAD (5.56 ± 0.77 ng/mL) in large compared to small microtumors (2.1 ± 0.32 ng/mL) by ELISA (Fig. 3E). Western blots revealed increased levels of sE-CAD and FN in 600/CM compared to small non-migratory mBC microtumors (Fig. 3F). Similarly, we observed significant upregulation of *FN* (2.5-fold) and *MMP9* (5-fold) in large compared to small microtumors of lung PDX (**dotted line,** Fig. 3G–H). ELISA and western blots showed high levels of sE-CAD and FN in the CM of large PDX (Fig. 3I–J) and mesothelioma microtumors (Supplementary Fig. S4D–E). Small lung PDX microtumors had non-detectable levels of sE-CAD measured by ELISA. These results indicate that our microtumor model can be easily adapted to patient- and xenograft-derived primary cancer cells across multiple tumor types such as breast, mesothelioma and lung tumors.

Mathematical model predicts a two-stage mechanism for microtumor progression and migration

Based on the above experimental findings and our previous study (25), we constructed a minimal regulatory network describing how microtumor migration is coupled to its microenvironment (Fig. 4A and Supplementary Fig. S5). Here, we focus on how the regulators including HIF-1α, MMP9, sE-CAD, and FN control the migratory phenotype. Increase in microtumor size leads to hypoxia, which stabilizes HIF-1α (37,38). HIF-1α can increase MMP9 expression (37), which can promote cleavage E-CAD to generate sE-CAD. Abnormally elevated levels of sE-CAD have been reported in various types of cancers (40,41). sE-CAD can bind and activate the epidermal growth factor receptor (EGFR) family (HER1–4), which further activates the ERK pathway (42–44) involved in the tumor cell proliferation. Moreover, pro-MMP9 and FN are targets of ERK-1/2 (9,44–46). For simplicity, these intermediate regulators (pro-MMP9, ERK-1/2) are taken implicitly in our minimal model. This completes a positive feedback loop among the microtumor-secreted factors, MMP9, sE-CAD and FN. We hypothesized that this positive feedback is critical for collective migration of microtumors. We built a mathematical model to describe the dynamics of these regulators with a set of ordinary differential equations (ODEs) as shown in Fig. 4B (see Supplementary material for details).

Through bifurcation analysis, we found that within a broad parameter range, the mathematical model gives an irreversible bistable switch. The level of [sE-CAD] is low in the CM of small microtumors (Fig. 4C, point 1). With increase in the tumor size, [sE-CAD] initially increases very slowly until a threshold (Saddle-Node bifurcation point, SN) of the microtumor size is reached, above which [sE-CAD] jumps to a higher value (Fig. 4C, point 2). Here, we used [sE-CAD] as a marker since it is experimentally straightforward to measure its levels and we have shown that the CM of migratory large microtumors contain higher [sE-CAD] than that of non-migratory small microtumors (Fig. 1D–E). It should be noted that this bistable switch is irreversible since [sE-CAD] remains high even after large microtumors are dissociated and re-grown as small ones (Fig. 4C, point 3), just as what we observed experimentally (Fig. 2A). The irreversibility of the switch is important for the collective migration since it implies that the cells in large microtumor can maintain their migratory phenotype even after escaping the hypoxic core or disaggregating from the tumor. This mathematical analysis suggests a two-stage tumor progression mechanism (Fig. 4A), where hypoxia is important in the early initiation stage of tumor progression, and components of the MMPs/sE-CAD/FN feedback loop work synergistically to maintain the migratory phenotype. Indeed, the modeling results in Fig. 4D predict that treatment with 600/CM (containing MMP9+sE-CAD, green line) or Rec-sE-CAD (blue line) shifts the threshold of microtumor size below 200μm for [sE-CAD] and tumor migration propensity. This was confirmed by our experimental results where treatment with 600/CM or Rec-sE-CAD induced migration in otherwise non-migratory 150μm microtumors (Fig. 2B–C). It is noted that patient-derived metastatic breast cancer (mBC) microtumors start to migrate before they reach 500–600μm in diameter (Supplementary Fig. S4A). That is, the threshold size for migration of these metastatic microtumors is lower than that of T47D microtumors. This may be due to the differences in the cell/tumor subtype, baseline phenotype of the cells, etc.

Our modeling studies reveal that a microtumor with size exceeding the critical value (SN) (Fig. 4C) generates and then maintains a microenvironment with high [sE-CAD] and starts to migrate. Due to stochasticity such as cell growth and division rates, the onset as well as the kinetics of individual microtumor migration may vary, which we refer to as 'dynamic inter-tumoral variation'. Fig. 4E shows simulated temporal dynamics of increase in [sE-CAD] in the CM of individual 150 and 600μm microtumors, where the dynamic inter-tumoral variation manifests itself, especially for the 600μm microtumors. Consequently, individual microtumors start to migrate at different times after day 2 (Fig. 4F), and within a range of microtumor sizes, our mathematical model predicts mixtures of migratory and non-migratory microtumors as we observed experimentally for T47D microtumors (Fig. 4G) (25). To reproduce our experimental results, we assumed that microtumor migration becomes visible when [sE-CAD] exceeds 80% of its steady state value with the corresponding time, $T_{migration}$ while the exact value of this threshold does not affect our conclusions in this work. The network in Fig. 4A suggests that one can inhibit microtumor migration by inhibiting regulators (HIF-1α/MMPs/sE-CAD) while inter-tumoral variation may complicate the outcomes. We present our modeling and experimental studies in the next sections.

Anti-hypoxia treatment attenuates microtumor migration most effectively only when HIF-1α is inhibited at early time points

Based on our two-stage progression mechanism, we hypothesized that inhibition of HIF-1α is most effective during the initialization stage. Figure 5A shows simulated time courses of [sE-CAD] without (black line) and with HIF-1α inhibitor treatment of 600μm microtumors at different times. The results show that a critical time exists (denoted as $T_{critical}$), where HIF-1α inhibition starting from T_1 ($T_1<T_{critical}$) can effectively prevent increase in [sE-CAD] (green line), thus inhibiting microtumor migration. In contrast, HIF-1α inhibition at T_2 ($T_2>T_{critical}$) cannot prevent further increase of already elevated [sE-CAD] (red line); hence the microtumor continues to migrate even in the presence of HIF-1α inhibitor. This implies that there is a treatment window (0 to $T_{critical}$) for HIF-1α inhibitor to be effective in restricting microtumor migration. Due to dynamic inter-tumoral variation, even microtumors of the same size have a distribution of $T_{critical}$ (Fig. 5B), which widens the boundary of this treatment window. Consequently, HIF-1α inhibition is effective in inhibiting migration in most of the microtumors when started before $T_{criticial}$ while some microtumors still migrate when the treatment is started on day 3 ($T_{critical}<T<T_{migration}$). HIF-1α inhibition from day 4 or day 5 ($T>T_{critical}$, $T_{migration}$) is not effective, showing migration in most of the microtumors (Fig. 5C–D). This implies that it is too late to stop migration with HIF-1α inhibition when the bistable switch is turned on by the hypoxic microenvironment. Together, computational modeling strongly suggests that although the hypoxic microenvironment induces the migratory phenotype, HIF-1α inhibition is effective only for a small time window of treatment and the window boundary is blurred by the existence of dynamic inter-tumoral variation.

To confirm our *in silico* results, we treated 600μm microtumors with the chemical inhibitor of HIF-1α starting on day 1 ($T < T_{critical}$, early inhibition), day 3 ($T_{critical}<T<T_{migration}$), day 4 or 5 ($T > T_{critical}$, $T_{migration}$, late inhibition) until day 6 of the culture. Interestingly,

HIF-1α inhibition from D1–6 or D3–6 inhibited microtumor migration significantly (only 3 and 11 out of 290 microtumors showed migration) (Fig. 5E–H). However, HIF-1α inhibition after day 4 (D4–6, D5–6) did not block migration similar to the untreated large microtumors (Fig. 5E–H, Supplementary Fig. S6A–B). The distance and extent of migration showed tumor-to-tumor variation as evident by the distribution and the wider error bars (Fig. 5G) and this variation correlated with the delay in starting the HIF-1α inhibitor treatment (Fig. 5G–H). Notably, these migratory microtumors continued to migrate even in presence of HIF-1α inhibitor (Fig. 5H, blue arrow, Supplementary Fig. S6).

The HIF-1α inhibition decreased [sE-CAD] from 13.1±1.8ng/mL (untreated controls) to 4.4±0.4ng/mL and 9.5±0.5ng/mL for D1–6 and D4–6 inhibition, respectively (Fig. 5I). Compared to the untreated microtumors, early (D1–6) HIF-1α inhibition decreased [sE-CAD] and FN in the 600/CM (Fig. 5J) and significantly downregulated *MMP9* (Fig. 5K), *VIM* and *FN* (Fig. 5L), without significant effect on *E-CAD* expression. Early HIF-1α inhibition also reduced pERK expression significantly compared to untreated control (Fig. 5M, Supplementary Fig. S6C). Although D4–6 HIF-1α inhibition reduced *FN* (both secreted in the CM and intracellular), this late inhibition could not reduce *MMP9* and *VIM* expression (Fig. 5K, L). These observations are consistent with and support our mathematical model reinforcing positive feedback loop between sE-CAD and MMP9 in the maintenance stage, and suggest that once established, such positive feedback may contribute to the ineffectiveness of HIF-1α inhibition.

Together, these results suggest that early HIF-1α inhibition ($T<T_{critical}$) can prevent microtumor migration while late inhibition ($T>T_{critical}$) does not work effectively. The results also support our hypothesis that hypoxia is important only for the initiation stage of microtumor migration and provide a mechanistic explanation for the clinical failure of anti-hypoxia treatments (18–20).

Blocking effects of sE-CAD by anti-sE-CAD antibody or preventing its shedding by MMP inhibitor effectively hinder microtumor migration

Our simulations predict that early ($T<T_{critical}$) sE-CAD inhibition will prevent/stop migration (Fig. 6A) by keeping [sE-CAD] low so that the bistable switch is not turned on to initiate the cascade necessary for microtumor migration. In the late inhibition ($T>T_{critical}$), although [sE-CAD] has exceeded the threshold causing some microtumors to migrate, sE-CAD inhibition turns the bistable switch off, and these microtumors cease to migrate further (Fig. 6A–B). That is, although fraction of migrated microtumor increases with the time of anti-sE-CAD treatment (Fig. 6B(i)), the fraction of continuously migrating microtumor disappears independent of time of anti-sE-CAD treatment (Fig. 6B(ii)). We obtained similar simulation results by inhibiting MMP-mediated sE-CAD shedding (Supplementary Fig. S7A–B). Together, these computational results suggest that unlike HIF-1α inhibition, the effectiveness of sE-CAD or MMP inhibition is independent of time of treatment and inter-tumoral variation.

To experimentally test the above model predictions, we blocked effects of sE-CAD in 600μm microtumors using antibody against the extracellular domain of E-CAD (H-108, Santa Cruz, 40μg/mL). Anti-sE-CAD antibody treatment scavenged the cleaved sE-CAD

and reduced the secreted FN in the CM compared to the untreated control (Fig. 6C, D). Anti-sE-CAD treatment on D3–6 completely inhibited collective migration (Supplementary Fig. S8A left panel). Although few microtumors treated with anti-sE-CAD antibody on D4–6 exhibited some migration (that was started before the treatment), the distance and extent of migration was significantly lower (38.4 ± 6.5μm and <25%, respectively) (Fig. 6E, F) compared to that achieved with HIF-1α inhibition on D4–6 (145.4 ± 25.3μm and 26–50%, respectively) (Fig. 5G–H). Indeed, the single microtumor trajectories clearly show that these already migrated microtumors stopped migration after anti-sE-CAD antibody treatment (Fig. 6F, blue arrow). The tight distribution of distance and extent of migration (Fig. 6E, F) also confirms our mathematical predictions that all treated microtumors respond similarly with minimal effect of inter-tumoral variation. These findings were further confirmed by qRT-PCR showing significant downregulation of *MMP9* (Fig. 6G) and *FN* (Fig. 6H) with no significant change in *VIM* and *E-CAD* after anti-sE-CAD antibody treatments. We observed similar results in primary mBC microtumors where anti-sE-CAD antibody treatment (D4–7) limited microtumor migration (Supplementary Fig. S8B), downregulated *MMP9* expression (Supplementary Fig. S8C) without altering mesenchymal marker expression (Supplementary Fig. S8D) and decreased sE-CAD levels (Supplementary Fig. S8E). This could be due to already elevated mesenchymal marker expression in mBC cells derived from metastatic tumors (Supplementary Fig. S3).

Additionally, we blocked sE-CAD shedding in 600μm microtumors by broad MMP inhibitor, GM6001 (20μM) on day 1 ($T<T_{critical}$) or day 4 ($T>T_{critical}$). MMP inhibition reduced sE-CAD shedding and secreted FN levels in the CM at both treatment times (Fig. 7A, B). *MMP9* mRNA expression was significantly downregulated at both treatment time points (Fig. 7C). We observed no migration for MMP inhibition started on day 1 whereas D4–6 treatment completely ceased the migration (Fig. 7D; Supplementary Fig. S7C). Early MMP inhibition ($T<T_{critical}$, D1–6) downregulated *VIM* and *FN* expression significantly without significant effect on *E-CAD* compared to untreated microtumors (Fig. 7E). On the other hand, late MMP inhibition ($T>T_{critical}$, D4–6) downregulated *FN* expression significantly without altering *VIM* expression similar to anti-sE-CAD treatment. MMP inhibition also reduced pERK/ERK ratio and ERK activation (Fig. 7F, Supplementary Fig. S7D). Notably, *VIM* expression was downregulated only with early inhibition of HIF-1α and MMPs in the initialization stage while it had no effect when these molecules were inhibited in the maintenance stage. MMP inhibition (D4–7) prevented migration in primary mBC microtumors (Supplementary Fig. S7E) and downregulated *MMP9* and *FN* expression along with decreased sE-CAD levels compared to untreated control (Supplementary Fig. S7F–H).

Together, experimental results in T47D and multiple primary patient-derived microtumors confirmed the predictions from our mathematical model. MMPs, sE-CAD, and FN are the components of the positive feedback loop and are critical to the irreversible bistable switch, and to maintain the microtumor migration. HIF-1α, on the other hand, is a major trigger of the switch, which is dispensable once the switch is turned on. These results confirmed our two-stage progression model that HIF-1α is important only in the initialization stage of tumor progression. Consequently, inhibiting HIF-1α is only effective before $T_{critical}$, which varies from tumor to tumor. Once MMPs, sE-CAD, and FN accumulate and exceed

threshold values, targeting these molecules is more effective in inhibiting microtumor migration, and has less constrains of the treatment time and dynamic tumor inter-tumoral variation.

Discussion

Solid tumor growth generates multiple layers of cells that build a physical barrier to diffusion of oxygen, nutrients and metabolites, leading to hypoxic tumor microenvironment, which further drives aggressive phenotype due to activation of various downstream signaling pathways (2,11,13). Hypoxic microenvironment further induces secretome, which contains many secreted factors, sheddases and proteases that reshape the tumor microenvironment, modulate cellular phenotypes, and affect drug responses (2,5,6,47). For in-depth mechanistic understanding of role of hypoxia and hypoxic secretome in inducing migratory phenotypes, it is desirable to have an experimental system that recapitulates spontaneously formed hypoxic microenvironment along with the tumor secretome because traditional 2D cell culture-based systems are unable to capture constantly evolving dynamic microenvironment (13).

To address this challenge, we engineered 3D microtumor models with controlled microenvironments to investigate the intricate core regulatory network implicated in inducing migration. We observed microtumor size-induced hypoxic signaling that leads to upregulation of mesenchymal markers and collective migration without loss of epithelial cadherin in large microtumors (25). The observed high levels of HIF-1α, MMPs, sE-CAD and FN in large microtumors suggest the interplay between hypoxia and hypoxic secretome for maintaining the migratory phenotype. Clinical data extracted from 3735 human breast tumor samples revealed higher levels of FN and MMP9 compared to normal mammary gland corroborating our findings. Through theoretical analysis with a minimal mathematical model, we proposed an irreversible bistable switch mechanism by which tumor cells migrate collectively once the microtumor grows larger than a pre-set threshold size. Our computational model successfully explained experimentally observed irreversible nature of the migratory phenotype in large microtumors and also predicted the efficacy of temporal inhibition of HIF-1α, MMPs and sE-CAD in halting microtumor migration. Different molecular species play temporally different roles in tumor progression, and proper choice of drug targets can minimize negative effects of such constantly evolving microenvironments on treatment efficacy (21,48). Indeed, through computational and experimental approaches, we predicted and validated a novel mechanism of two-stage tumor progression where hypoxia is critical in initiating the migratory phenotype, which is then maintained by tumor-secreted factors such as MMPs, sE-CAD and FN. We acknowledge that the proposed mathematical model of regulatory network is far from complete to characterize all the changes required for induction of tumor migration. The transcriptomic and proteomic profiles of these complementary 3D models (hypoxic and migratory large microtumors, non-hypoxic non-migratory small microtumors and hypoxic CM- treated non-hypoxic yet migratory small microtumors) will provide more complete mechanistic insights in our future study.

Since the hypoxia-induced HIF-1α plays an important role only at the initial stage of activating the bistable switch, HIF-1α inhibition can effectively halt tumor migration only if treated prior to the onset of migratory phenotypes ($T<T_{migration}$), which is not easy in practice due to the stochastic dynamics of tumor growth. This further explains failure of HIF-1α inhibition strategies to stop tumor progression in clinics, as it may be too late to stop the entire signaling cascade induced by HIF-1α in already hypoxic tumors. Both our computational and experimental studies demonstrate that efficacy of HIF-1α inhibition to prevent tumor migration is significantly affected by treatment initiation time and inter-tumoral variation leading to variable treatment efficacy, consistent with the conflicting results observed in the clinical studies (18–20).

Our mathematical prediction of two-stage progression mechanism suggests that the sE-CAD/MMP/FN axis mainly functions to maintain the migratory phenotype, and its inhibition is less affected by the stochastic tumor growth. Experimentally, inhibition of sE-CAD by MMP inhibitor or by anti-E-CAD antibody, both suppressed the collective migration in T47D and primary patient-derived microtumors. Unlike HIF-1α inhibition, sE-CAD inhibition was much less affected by inter-tumoral variation. We propose sE-CAD as a potential target since it seems not to have an essential physiological role (49), pharmaceutical intervention to keep sE-CAD below a threshold level may not increase toxicity of concurrent anti-neoplastic regimens. Further, unlike the treatment strategies targeting inhibition of tumor growth, the strategy proposed here of targeting tumor-secreted factors to constrain tumor migration may impose much less selection pressure as predicted from cancer evolutionary theory (50).

Another important aspect of this study is our ability to cross-examine roles of different regulators such as pharmacological inhibition in hypoxic, migratory large microtumors and stimulation/induction in non-hypoxic, non-migratory small microtumors, using complementary, yet controlled model systems made of the same parent cells. For instance, inhibition of sE-CAD by anti-E-CAD antibody stops migration in large hypoxic microtumors by downregulating *FN*, but without affecting *VIM* expression. Also, stimulation with human Rec-sE-CAD induces collective migration and *FN* upregulation in non-hypoxic, non-migratory small microtumors without affecting *VIM* expression, suggesting that sE-CAD is not an effective regulator of *VIM,* and *VIM* is dispensable for migration. The role of epithelial and mesenchymal phenotypes in cancer cell migration has been widely debated in recent years (3,51,52). Our results suggest co-existence of multiple distinct phenotypes as indicated by differential expression patterns of *VIM* and *FN*, and these phenotypes cannot be sufficiently characterized by individual mesenchymal marker as in the two controversial studies (51,52). Further studies are needed to examine whether these phenotypes actively contribute to migration or are simply passive outcomes of the microenvironment.

In summary, our combined experimental and mathematical modeling studies demonstrate the importance of taking into account the temporal dynamics of evolving tumor microenvironments, resonant with other studies stressing dynamic pharmacology (53). We provide insight into how HIF-1α, MMP, E-CAD, and FN work together to generate emergent properties, more specifically, the irreversibility of the migratory phenotype, and

provide evidence that it is more effective and practical to target network components (e.g., sE-CAD) that control the migratory phenotype maintenance instead of those (e.g., HIF-1α) for the initialization stage. While in this work, we focused on a few tumor-secreted factors, both our experimental system and computational approach can be readily applied to include couplings between the secretome network and intracellular signal transduction and gene regulation networks. The microtumor models can uniquely provide quantitative information of the temporal evolution of both, the microenvironment and cell phenotypes in an approachable experimental setting, and identify combined therapeutic strategies that overcome problems of drug resistance of existing ones (21,47).

Supplementary Material

Refer to Web version on PubMed Central for supplementary material.

Acknowledgments

We thank Dr. Wen Xie, University of Pittsburgh School of Pharmacy, for providing access to the core facilities. We thank Drs. Barry Gold and Vinayak Sant, Department of Pharmaceutical Sciences, for critical reading and insightful suggestions on the manuscript. This work is supported by the Department of Pharmaceutical Sciences, School of Pharmacy University of Pittsburgh (SS), NIH (R37CA232209; SS, JX, VSD, SCW), the National Science Foundation (DMS-1462049; JX); the Pennsylvania Department of Health (SAP 4100062224, JX); BC032981, BC044784, W81XWH-12-1-0415 and BC132245_W81XWH-14-0258 from the Department of Defense (VSD), the Hillman Foundation (VSD) and the Glimmer of Hope Foundation (VSD). The confocal microscope in the Center for Biologic Imaging at University of Pittsburgh is UPCI supported by 1S10OD019973–01 to SCW. Cytometry Facility is supported by CCSG P30CA047904.

References

1. Gilkes DM, Semenza GL, Wirtz D. Hypoxia and the extracellular matrix: drivers of tumour metastasis. Nature reviews Cancer 2014;14:430–9 [PubMed: 24827502]
2. Rankin EB, Giaccia AJ. Hypoxic control of metastasis. Science (New York, NY) 2016;352:175–80
3. Nieto MA, Huang RY, Jackson RA, Thiery JP. EMT: 2016. Cell 2016;166:21–45 [PubMed: 27368099]
4. Cheung KJ, Ewald AJ. Illuminating breast cancer invasion: diverse roles for cell-cell interactions. Current opinion in cell biology 2014;30:99–111 [PubMed: 25137487]
5. Miller MA, Oudin MJ, Sullivan RJ, Wang SJ, Meyer AS, Im H, et al. Reduced Proteolytic Shedding of Receptor Tyrosine Kinases Is a Post-Translational Mechanism of Kinase Inhibitor Resistance. Cancer discovery 2016;6:382–99 [PubMed: 26984351]
6. Karagiannis GS, Pavlou MP, Diamandis EP. Cancer secretomics reveal pathophysiological pathways in cancer molecular oncology. Molecular oncology 2010;4:496–510 [PubMed: 20934395]
7. Cox TR, Rumney RMH, Schoof EM, Perryman L, Hoye AM, Agrawal A, et al. The hypoxic cancer secretome induces pre-metastatic bone lesions through lysyl oxidase. Nature 2015;522:106–10 [PubMed: 26017313]
8. Brouxhon SM, Kyrkanides S, Teng X, Raja V, O'Banion MK, Clarke R, et al. Monoclonal antibody against the ectodomain of E-cadherin (DECMA-1) suppresses breast carcinogenesis: involvement of the HER/PI3K/Akt/mTOR and IAP pathways. Clinical cancer research : an official journal of the American Association for Cancer Research 2013;19:3234–46 [PubMed: 23620408]
9. Overall CM, Lopez-Otin C. Strategies for MMP inhibition in cancer: innovations for the post-trial era. Nature reviews Cancer 2002;2:657–72 [PubMed: 12209155]
10. Paltridge JL, Belle L, Khew-Goodall Y. The secretome in cancer progression. Biochimica et Biophysica Acta (BBA) - Proteins and Proteomics 2013;1834:2233–41 [PubMed: 23542208]
11. Kao SH, Wu KJ, Lee WH. Hypoxia, Epithelial-Mesenchymal Transition, and TET-Mediated Epigenetic Changes. Journal of clinical medicine 2016;5 [PubMed: 28465746]

12. Grigore AD, Jolly MK, Jia D, Farach-Carson MC, Levine H. Tumor Budding: The Name is EMT. Partial EMT. Journal of clinical medicine 2016;5 [PubMed: 28465746]
13. Nobre AR, Entenberg D, Wang Y, Condeelis J, Aguirre-Ghiso JA. The Different Routes to Metastasis via Hypoxia-Regulated Programs. Trends in cell biology 2018;28:941–56 [PubMed: 30041830]
14. Tian XJ, Zhang H, Xing J. Coupled reversible and irreversible bistable switches underlying TGFbeta-induced epithelial to mesenchymal transition. Biophysical journal 2013;105:1079–89 [PubMed: 23972859]
15. Zhang J, Tian XJ, Zhang H, Teng Y, Li R, Bai F, et al. TGF-beta-induced epithelial-to-mesenchymal transition proceeds through stepwise activation of multiple feedback loops. Science signaling 2014;7:ra91 [PubMed: 25270257]
16. Young SD, Marshall RS, Hill RP. Hypoxia induces DNA overreplication and enhances metastatic potential of murine tumor cells. Proceedings of the National Academy of Sciences of the United States of America 1988;85:9533–7 [PubMed: 3200838]
17. Young SD, Hill RP. Effects of Reoxygenation on Cells From Hypoxic Regions of Solid Tumors: Anticancer Drug Sensitivity and Metastatic Potential. JNCI: Journal of the National Cancer Institute 1990;82:371–80 [PubMed: 2304086]
18. Mack PC, Redman MW, Chansky K, Williamson SK, Farneth NC, Lara PN, et al. Lower osteopontin plasma levels are associated with superior outcomes in advanced non-small-cell lung cancer patients receiving platinum-based chemotherapy: SWOG Study S0003. J Clin Oncol 2008;26:4771–6 [PubMed: 18779603]
19. Patel A, Sant S. Hypoxic tumor microenvironment: Opportunities to develop targeted therapies. Biotechnology advances 2016;34:803–12 [PubMed: 27143654]
20. Williamson SK, Crowley JJ, Lara PN, McCoy J, Lau DHM, Tucker RW, et al. Phase III Trial of Paclitaxel Plus Carboplatin With or Without Tirapazamine in Advanced Non–Small-Cell Lung Cancer: Southwest Oncology Group Trial S0003. Journal of Clinical Oncology 2005;23:9097–104 [PubMed: 16361616]
21. Donnenberg VS, Donnenberg AD. Stem cell state and the epithelial-to-mesenchymal transition: Implications for cancer therapy. Journal of clinical pharmacology 2015;55:603–19 [PubMed: 25708160]
22. Gong X, Lin C, Cheng J, Su J, Zhao H, Liu T, et al. Generation of Multicellular Tumor Spheroids with Microwell-Based Agarose Scaffolds for Drug Testing. PloS one 2015;10:e0130348 [PubMed: 26090664]
23. Nyberg SL, Hardin J, Amiot B, Argikar UA, Remmel RP, Rinaldo P. Rapid, large-scale formation of porcine hepatocyte spheroids in a novel spheroid reservoir bioartificial liver. Liver transplantation : official publication of the American Association for the Study of Liver Diseases and the International Liver Transplantation Society 2005;11:901–10
24. Sant S, Johnston PA. The production of 3D tumor spheroids for cancer drug discovery. Drug Discov Today Technol 2017;23:27–36 [PubMed: 28647083]
25. Singh M, Mukundan S, Jaramillo M, Oesterreich S, Sant S. Three-Dimensional Breast Cancer Models Mimic Hallmarks of Size-Induced Tumor Progression. Cancer research 2016;76:3732–43 [PubMed: 27216179]
26. Singh M, Close DA, Mukundan S, Johnston PA, Sant S. Production of Uniform 3D Microtumors in Hydrogel Microwell Arrays for Measurement of Viability, Morphology, and Signaling Pathway Activation. Assay and drug development technologies 2015;13:570–83 [PubMed: 26274587]
27. Singh M, Warita K, Warita T, Faeder JR, Lee REC, Sant S, et al. Shift from stochastic to spatially-ordered expression of serine-glycine synthesis enzymes in 3D microtumors. Scientific Reports 2018;8:9388 [PubMed: 29925909]
28. Singh M, Venkata Krishnan H, Ranganathan S, Kiesel B, Beumer JH, Sreekumar S, et al. Controlled three-dimensional tumor microenvironments recapitulate phenotypic features and differential drug response in early vs. advanced stage breast cancer. ACS Biomaterials Science & Engineering 2017

29. Donnenberg VS, Donnenberg AD, Zimmerlin L, Landreneau RJ, Bhargava R, Wetzel RA, et al. Localization of CD44 and CD90 positive cells to the invasive front of breast tumors. Cytometry Part B, Clinical cytometry 2010;78:287–301
30. Donnenberg VS, Landreneau RJ, Pfeifer ME, Donnenberg AD. Flow cytometric determination of stem/progenitor content in epithelial tissues: an example from nonsmall lung cancer and normal lung. Cytometry Part A : the journal of the International Society for Analytical Cytology 2013;83:141–9 [PubMed: 23081669]
31. Susaki EA, Tainaka K, Perrin D, Kishino F, Tawara T, Watanabe TM, et al. Whole-brain imaging with single-cell resolution using chemical cocktails and computational analysis. Cell 2014;157:726–39 [PubMed: 24746791]
32. Watson AM, Rose AH, Gibson GA, Gardner CL, Sun C, Reed DS, et al. Ribbon scanning confocal for high-speed high-resolution volume imaging of brain. PloS one 2017;12:e0180486 [PubMed: 28686653]
33. Frankowski H, Gu YH, Heo JH, Milner R, Del Zoppo GJ. Use of gel zymography to examine matrix metalloproteinase (gelatinase) expression in brain tissue or in primary glial cultures. Methods in molecular biology (Clifton, NJ) 2012;814:221–33
34. Espina V, Liotta LA. What is the malignant nature of human ductal carcinoma in situ? Nature reviews Cancer 2011;11:68–75 [PubMed: 21150936]
35. De Sousa EMF, Vermeulen L, Fessler E, Medema JP. Cancer heterogeneity--a multifaceted view. EMBO reports 2013;14:686–95 [PubMed: 23846313]
36. Khalil AA, Ilina O, Gritsenko PG, Bult P, Span PN, Friedl P. Collective invasion in ductal and lobular breast cancer associates with distant metastasis. Clin Exp Metastasis 2017;34:421–9 [PubMed: 28894989]
37. Choi JY, Jang YS, Min SY, Song JY. Overexpression of MMP-9 and HIF-1alpha in Breast Cancer Cells under Hypoxic Conditions. Journal of breast cancer 2011;14:88–95 [PubMed: 21847402]
38. Chua YL, Dufour E, Dassa EP, Rustin P, Jacobs HT, Taylor CT, et al. Stabilization of hypoxia-inducible factor-1alpha protein in hypoxia occurs independently of mitochondrial reactive oxygen species production. The Journal of biological chemistry 2010;285:31277–84 [PubMed: 20675386]
39. Brouxhon SM, Kyrkanides S, Teng X, Athar M, Ghazizadeh S, Simon M, et al. Soluble E-cadherin: a critical oncogene modulating receptor tyrosine kinases, MAPK and PI3K/Akt/mTOR signaling. Oncogene 2014;33:225–35 [PubMed: 23318419]
40. David JM, Rajasekaran AK. Dishonorable discharge: the oncogenic roles of cleaved E-cadherin fragments. Cancer research 2012;72:2917–23 [PubMed: 22659456]
41. Repetto O, De Paoli P, De Re V, Canzonieri V, Cannizzaro R. Levels of Soluble E-Cadherin in Breast, Gastric, and Colorectal Cancers. BioMed Research International 2014;2014:408047 [PubMed: 25535613]
42. Najy AJ, Day KC, Day ML. The ectodomain shedding of E-cadherin by ADAM15 supports ErbB receptor activation. The Journal of biological chemistry 2008;283:18393–401 [PubMed: 18434311]
43. Inge LJ, Barwe SP, D'Ambrosio J, Gopal J, Lu K, Ryazantsev S, et al. Soluble E-cadherin promotes cell survival by activating epidermal growth factor receptor. Experimental cell research 2011;317:838–48 [PubMed: 21211535]
44. Brouxhon SM, Kyrkanides S, Teng X, O'Banion MK, Clarke R, Byers S, et al. Soluble-E-cadherin activates HER and IAP family members in HER2+ and TNBC human breast cancers. Molecular carcinogenesis 2014;53:893–906 [PubMed: 23776059]
45. Grabowska MM, Sandhu B, Day ML. EGF promotes the shedding of soluble E-cadherin in an ADAM10-dependent manner in prostate epithelial cells. Cellular Signalling 2012;24:532–8 [PubMed: 22024284]
46. Moshal KS, Sen U, Tyagi N, Henderson B, Steed M, Ovechkin AV, et al. Regulation of homocysteine-induced MMP-9 by ERK1/2 pathway. American journal of physiology Cell physiology 2006;290:C883–91 [PubMed: 16251475]
47. Miller MA, Sullivan RJ, Lauffenburger DA. Molecular Pathways: Receptor Ectodomain Shedding in Treatment, Resistance, and Monitoring of Cancer. Clinical cancer research : an official journal of the American Association for Cancer Research 2017;23:623–9 [PubMed: 27895032]

48. Schmidt KT, Chau CH, Price DK, Figg WD. Precision Oncology Medicine: The Clinical Relevance of Patient-Specific Biomarkers Used to Optimize Cancer Treatment. Journal of clinical pharmacology 2016;56:1484–99 [PubMed: 27197880]

49. Grabowska MM, Day ML. Soluble E-cadherin: more than a symptom of disease. Frontiers in bioscience (Landmark edition) 2012;17:1948–64 [PubMed: 22201848]

50. Greaves M, Maley CC. Clonal evolution in cancer. Nature 2012;481:306–13 [PubMed: 22258609]

51. Zheng X, Carstens JL, Kim J, Scheible M, Kaye J, Sugimoto H, et al. Epithelial-to-mesenchymal transition is dispensable for metastasis but induces chemoresistance in pancreatic cancer. Nature 2015;527:525–30 [PubMed: 26560028]

52. Fischer KR, Durrans A, Lee S, Sheng J, Li F, Wong STC, et al. Epithelial-to-mesenchymal transition is not required for lung metastasis but contributes to chemoresistance. Nature 2015;527:472–6 [PubMed: 26560033]

53. Behar M, Barken D, Werner SL, Hoffmann A. The Dynamics of Signaling as a Pharmacological Target. Cell 2013;155:448–61 [PubMed: 24120141]

Significance:

This study uses state-of-the-art three-dimensional (3D) microtumor models and computational approaches to highlight the temporal dynamics of tumor-secreted microenvironmental factors in inducing tumor migration.

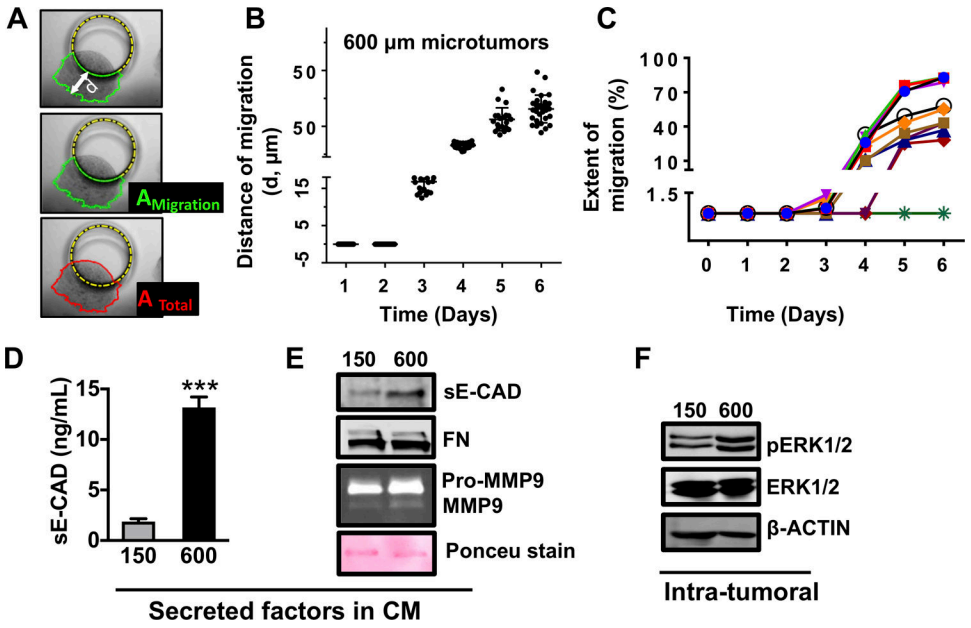

Figure 1: Large microtumors exhibit hypoxia, collective migration and aggressive phenotype.

(A) Schematic defining distance of migration (d), area of microtumor migrated out of the microwell ($A_{Migration}$) and total area of the microtumor (A_{Total}); (B) Distance of migration for individual microtumors; each dot represents data for individual microtumor. (C) Migration trajectories of individual 600μm microtumors from day 1 to day 6 showing inter-tumoral variation in migration kinetics; Extent of migration for each time point was calculated as migrated distance/the total area of microtumor X 100. Levels of sE-CAD (D, ELISA) and sE-CAD, FN, Pro-MMP9 and MMP9 (E, western blot) in CM; (F) pERK expression in microtumor cell lysates. Data presented is representative from three independent experiments (n=3). ***p<0.001, p****< 0.0001; Unpaired t-test.

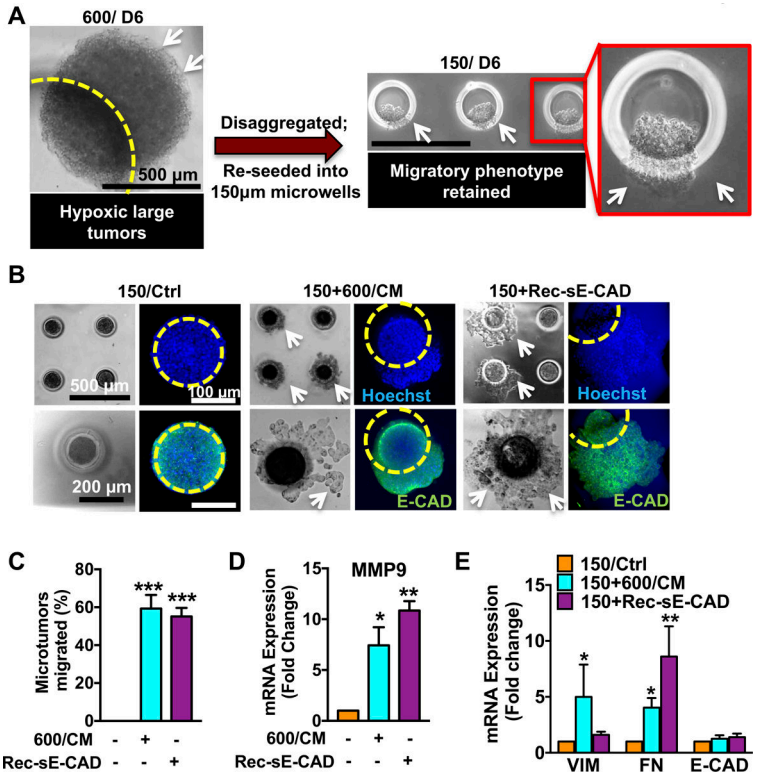

Figure 2. Recombinant sE-CAD and hypoxic secretome (CM) induce collective migration in non-migratory 150μm microtumors.

(A) 600μm microtumors maintained their migratory phenotype (white arrows) even after disrupting hypoxia (disaggregation) and re-growing them into non-hypoxic 150μm microtumors (Inset). (B) Representative images showing collective migration (white arrows) in 600/CM and Rec-sE-CAD-treated 150μm microtumors without loss of E-CAD (green), blue: cell nuclei and yellow circle: boundary of a microwell. Effect of 600/CM and Rec-sE-CAD treatments on migration (C) and mRNA expression of (D) MMP9 and (E) VIM, FN and E-CAD in treated 150μm microtumors. Data are presented as mean ± SD (C) and mean ± SEM (D,E) from three independent experiments. *p<0.05, **p<0.01, ***p<0.001 w.r.t. untreated 150μm microtumors.

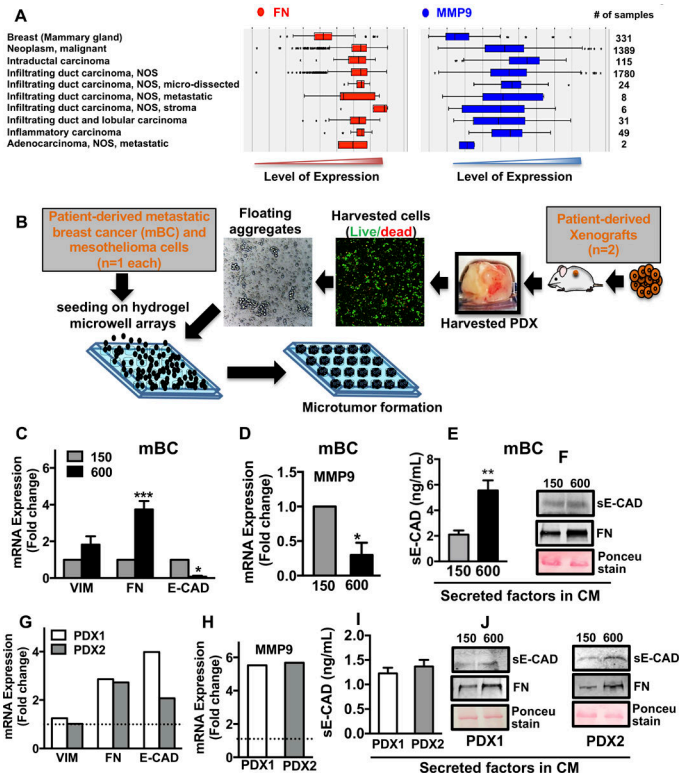

Figure 3. Tumor secretome in patient tumors, microtumors of primary tumors and PDX cells showed upregulation of FN, MMP9 and sE-CAD.

(A) Analysis of clinical data set showed higher levels of FN and MMP9 in breast carcinomas compared to normal mammary gland. (B) Hydrogel microwell arrays (150 and 600μm) were used to generate the microtumors from patient-derived primary metastatic breast cancer (mBC) cells (1 patient), mesothelioma cells (1 patient) and non-small cell lung cancer PDX model (2 PDX tumors). Analysis of mRNA expression of (C) VIM, FN, E-CAD and (D) MMP9; protein levels of sE-CAD (E,F) and FN (F) in the mBC cell-derived microtumors and similarly, in the PDX cell-derived microtumors (G-J). Dotted line in G, H refers to expression in small microtumors; non-detectable sE-CAD levels in small microtumors (I). *p<0.05, **p<0.01, ***p<0.001, Unpaired t-test.

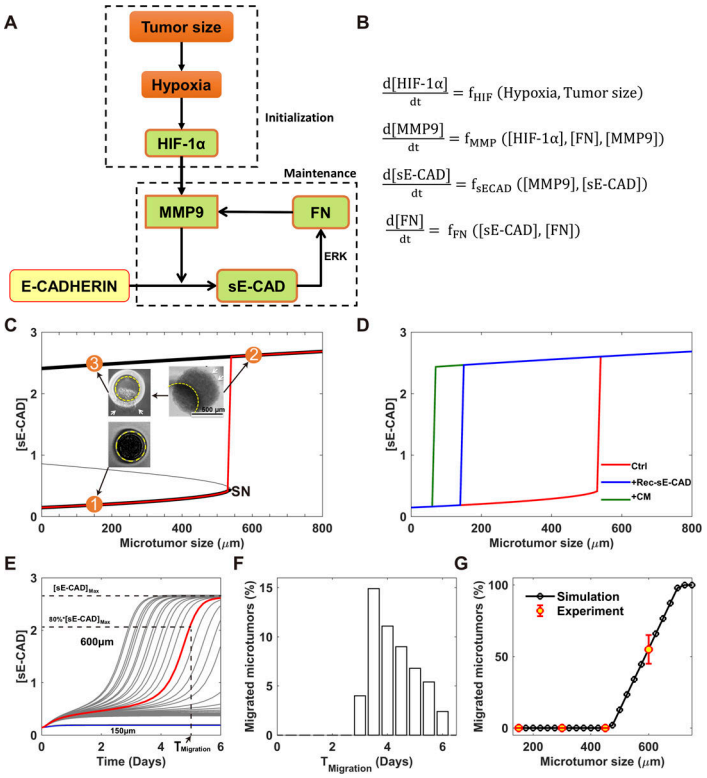

Figure 4. Mathematical model predicts an irreversible bistable switch as the mechanism of the migratory behavior of the microtumor.

(A) Schematic depiction of the core regulatory network. (B) The corresponding mathematical model described with ordinary differential equations (ODE) (details in the Supplemental Information); (C) Bifurcation analysis of the mathematical model gives an irreversible bistable switch. There is a threshold (SN) of microtumor size for the activation of this switch. Case 1: 150μm microtumor does not exceed the threshold and does not migrate. Case 2: Hypoxic microenvironment in 600μm microtumor exceeds the threshold and induces high levels of [sE-CAD] and a migratory phenotype. Case 3: Re-growing 600μm microtumors into non-hypoxic small microtumors still maintains high [sE-CAD] and migratory phenotype suggesting irreversibility of the switch; (D) The threshold of microtumor size for migration shifts to lower sizes (< 200μm) in the presence of Rec-sE-CAD (blue) or CM from migrated microtumor (green); (E) The heterogeneous dynamics of the [sE-CAD] for 150 and 600μm microtumors due to the inter-tumoral variation (n=30 microtumors for each size). It is assumed that the microtumor migration becomes visible when [sE-CAD] exceeds 80% of its steady state value with the corresponding time, $T_{migration}$. Unlike 600μm microtumors, 150μm microtumors have negligible variation; (F) The distribution of $T_{migration}$ (n=1000 microtumors); (G) Simulation and experimental data reveal that the percentage of the migrated microtumors depends on the microtumor size.

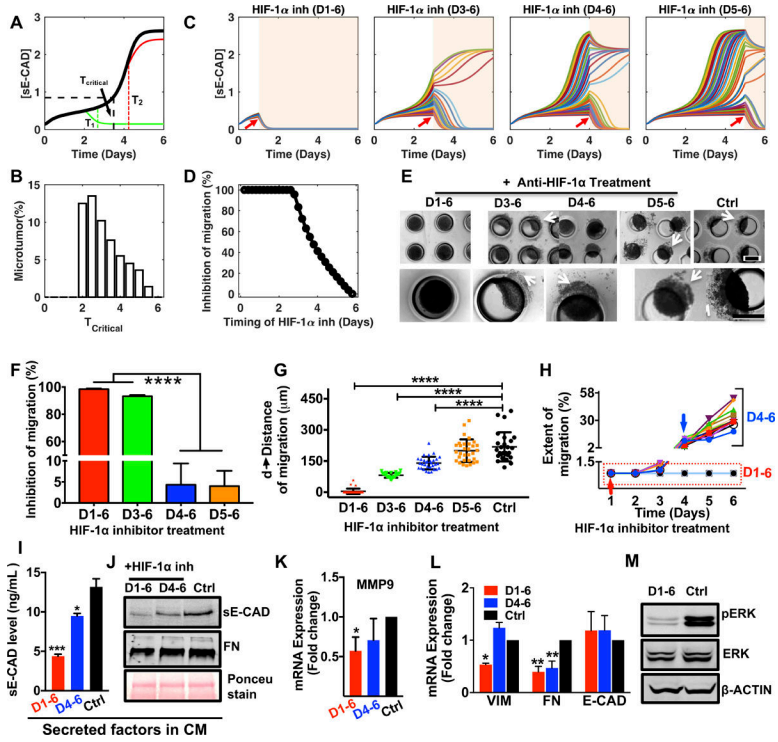

Figure 5: HIF-1α inhibition effectively attenuates microtumor migration only when HIF-1α is inhibited at early time points.

(A) Mathematical model predicts a critical time ($T_{critical}$) to stop migration with HIF-1α inhibition for single microtumor. HIF-1α inhibition can attenuate microtumor migration (green) only if treated before the critical time (T1), but has no effect after the critical time (T2, red line); (B) Distribution of $T_{critical}$ (n=1000 microtumors) emphasizes inter-tumoral variation; (C) Dynamics of [sE-CAD] under HIF-1α inhibition at different times (n=50 microtumors for each case). Treatment periods shaded with light background. (D) HIF-1α inhibition started before day 3 inhibits microtumor migration significantly (n=1000 microtumors); (E) Photomicrographs show migratory status of 600μm microtumors on day 6 with HIF-1α inhibition at different times. The effect of HIF-1α inhibition on microtumor migration (F), distance of migration (G), and extent of migration (H). Each dot in G represents data for individual microtumor. Each line in H represents migration kinetics for individual microtumor with HIF-1α inhibition on day 1 (red arrow) or day 4 (blue arrow). HIF-1α inhibition (D1–6) downregulated (I) sE-CAD levels (ELISA), (J) sE-CAD and FN expression (western blot) in 600/CM, downregulated mRNA expression of (K) MMP9; (L) VIM and FN; and protein expression of (M) pERK. Data is presented as mean ± SEM. *p<0.05, **p<0.01, ****p< 0.0001 w.r.t. untreated 600μm microtumors; One-way ANOVA followed by Tukey's test.

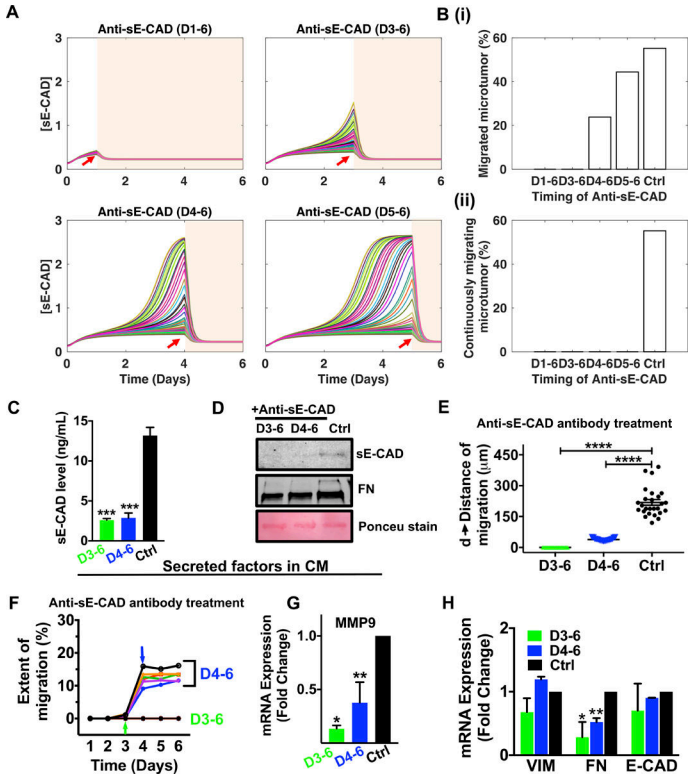

Figure 6. Inhibition of sE-CAD by anti-E-CAD antibody attenuated collective migration in 600μm microtumors.

(A) The dynamics of [sE-CAD] in 50 microtumors post anti-sE-CAD antibody treatment started on day 1, day 3, day 4 and day 5 (red arrows); (B) The fraction of migrated microtumors (upper panel, i) and continuously migrating microtumors (lower panel, ii) with anti-sE-CAD antibody treatment (n=1000 microtumors). Anti-sE-CAD antibody treatment (40μg/mL) on day 3 and 4 reduced (C) sE-CAD levels (ELISA), (D) sE-CAD and FN expression (western blot) in 600/CM, reduced (E) distance of migration, (F) extent of migration, and downregulated mRNA expression of MMP9 (G) and FN (H). Data are drawn from three independent experiments and are presented as means ± SEM. p*<0.05, **p<0.01, ***p<0.001 w.r.t. untreated control; One-way ANOVA followed by Tukey's test.

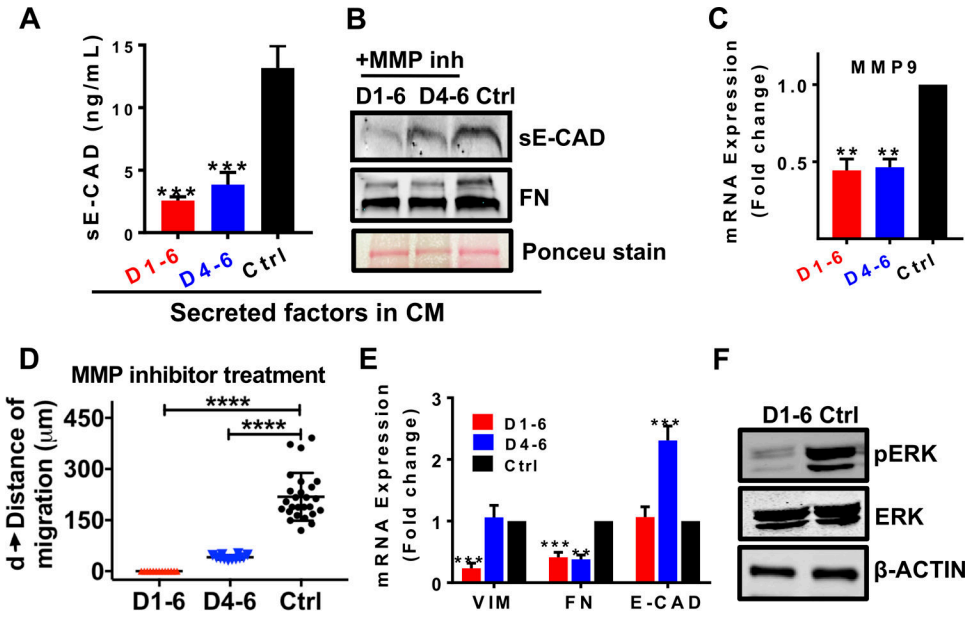

Figure 7. MMP inhibitor treatment attenuated collective migration in a time-independent manner.

MMP inhibitor treatment (20μM of GM6001) on day 1–6 and day 4–6 decreased (A) sE-CAD levels (ELISA), (B) sE-CAD and FN expression (western blot) in 600/CM, (C) downregulated MMP9 mRNA expression, (D) inhibited migration significantly, (E) downregulated VIM and FN mRNA expression, and (F) pERK microtumors compared to untreated controls. Data is presented as means ± SEM from 3 independent experiments. **p<0.01, ***p<0.001, ****p<0.0001; w.r.t. untreated control; One-way ANOVA followed by Tukey's test.